JVST B
Journal of Vacuum Science & Technology B

ARTICLE

avs.scitation.org/journal/jvb

Angular dependence of secondary electron yield from microporous gold surfaces

Cite as: J. Vac. Sci. Technol. B 38, 054001 (2020); doi: 10.1116/6.0000346
Submitted: 20 May 2020 · Accepted: 16 July 2020 ·
Published Online: 10 August 2020

Jonathan Ludwick,[1,a)] Asif Iqbal,[2] Daniel Gortat,[3] John D. Cook,[3] Marc Cahay,[1] Peng Zhang,[2] Tyson C. Back,[4] Steven Fairchild,[4] Martin Sparkes,[3] and William O'Neill[3]

AFFILIATIONS

[1]College of Engineering and Applied Science, University of Cincinnati, Cincinnati, Ohio 45221
[2]Department of Electrical and Computer Engineering, Michigan State University, East Lansing, Michigan 48824
[3]Institute for Manufacturing, University of Cambridge, Cambridge CB3 0FS, United Kingdom
[4]Air Force Research Laboratory, Materials and Manufacturing Directorate, Wright-Patterson Air Force Base, Ohio 45433

[a)]**Author to whom correspondence should be addressed:** ludwicjb@mail.uc.edu

ABSTRACT

We report exhaustive measurements of the secondary electron yield (SEY) from a gold film containing an array of micropores as a function of the angle of incidence of the primary electrons. The SEY measurements are in good agreement with Monte-Carlo (MC) simulations. A highly accurate empirical fit to the SEY data as a function of the incident electron impact angle is also proposed. In this study, the micropores have aspect ratios (ratio of pore height over pore diameter) ranging from about 1.5 to 3.5. The effect of the pore array density (porosity) and pore aspect ratio is analyzed in greater detail. It is found that increasing the pore aspect ratio and porosity leads to a sharp reduction in the total SEY in agreement with MC simulations.

I. INTRODUCTION

Secondary electron emission (SEE) occurs when an incident electron of an arbitrary kinetic energy strikes the surface of a material and generates secondary electrons that emit from the surface. SEE is a well-known root cause for performance efficiency reduction or even device failure in high powered vacuum electronics (HPVE) and particle accelerators due to effects such as the electron cloud effect,[1] electrostatic discharge,[2] and the multipactor effect.[3–7] Various materials intrinsically have different secondary electron yield (SEY) magnitudes, as reported from a variety of sources over the past century.[8] Reducing the SEE to avoid the aforementioned unwanted secondary effects in the particle accelerator and HPVE systems can be achieved by simply using materials with lower SEYs. However, if material replacement is not an option, altering the surface topography of materials is another viable method to reduce SEY. Previous work has successfully shown SEY reduction from grooved surfaces,[9] arrays of shallow cylindrical micropores,[10–13] and arrays of deep cylindrical micropores.[14] Here, we define shallow and deep micropores as having aspect ratios (ARs) of less than and greater than 1.0, respectively, where AR is defined as the micropore depth divided by the diameter.

Previous research on deep micropores[14] only accounts for normally incident electrons inducing SEE. However, in real devices, incident electrons induce SEE with a variety of incident angles. These different incident angles will have a significant impact on the SEY reduction effectiveness of the deep microporous array. It is, therefore, critical to extend the deep micropore research to understand the influence of the incident electron impact angle.

This work studies the angular SEY dependence of deep microporous arrays on gold surfaces. These deep microporous arrays were first fabricated on 304SS surfaces, and then a thin gold film was deposited on their surfaces. The microporous samples were fabricated using a laser drilling technique at the University of Cambridge. The SEY from these surfaces was then measured at the Materials and Manufacturing Directorate at the Air Force Research Laboratory (AFRL/RXAP). Finally, an empirical model and a Monte-Carlo (MC) simulation tool to predict the SEY of microporous samples were developed at the Michigan State University.

TABLE I. Numbered gold coated samples with hole specifications (μm). The hole depth across all samples was 59.9 μm.

Sample	Hole radius	Hole-hole distance	Aspect ratio	Porosity	Array
1	9.9	50	3.0	0.14	Hexagonal
2	8.5	50	3.5	0.18	Square
3	19	81	1.5	0.21	Hexagonal
4	18	60	1.6	0.33	Hexagonal
5	9.9	30	3.0	0.40	Hexagonal
6	8.5	30	3.5	0.50	Square
7	21	44	1.5	0.80	Hexagonal
8	20	38	1.5	1.0	Hexagonal
9	18	33	1.7	1.0	Hexagonal
10	16	28	1.9	1.1	Hexagonal

II. SAMPLE FABRICATION

This section addresses the manufacturing steps taken to produce the microporous 304SS samples with a 100 nm deposited gold film shown in Table I.

The hole porosity was calculated using the formula in Fig. 1. The micropores begin to overlap one another when the porosities exceed 0.907 and 0.785 for the hexagonal and square array samples, respectively. The array types (square and hexagonal) are assumed to have no effect on the SEY physics. Their only function is to allow different pore packing densities during fabrication.

A. Fabrication process

At the University of Cambridge, samples of 304SS were cleaned with acetone and irradiated at the normal incidence by a circularly polarised laser beam. The laser system used was a linearly polarized Amplitude Systemes Satsuma ultrafast laser, of wavelength of 1030 nm, >300 fs pulse duration, beam quality factor (representing the degree of variation of a beam from an ideal Gaussian beam) of $M^2 < 1.1$ and maximum output power of 5 W, raw beam diameter of 4.4 mm with a 12.7 mm focal length lens, and an effective spot diameter of 4.1 μm. To achieve circular polarization, a $\lambda/4$ wave plate was placed in the beam path. The experiments were conducted in ambient air at room temperature. To ensure that the samples would not move during machining, they were fixed with a double sided sticky tape to the moving XY stage, as shown in Fig. 2. For perpendicular alignment to the laser beam, the samples were placed on a Thorlabs pitch and roll stage. N_2 was used as the shielding gas for the lens against the drilling debris. The laser was focused on the substrate via a 3-axis Aerotech stage. The number of pulses was controlled with a pulse synchronized output of the laser. The laser setup is illustrated in Fig. 2.

To avoid fluctuations in pore diameters, the sample surface must be flat prior to drilling. The flatness of the samples was measured by machining laser lines at variable focus points in the center and four corners of the surface of the sample. Each pattern had a 20 μm incremental offset perpendicular to the sample surface, passing through the focal point. All the lines must be of equal width when measured with the Dino microscope *in situ* in the center and four corners of the surface of the sample. This method

$$\rho = \frac{pore\ area}{hexagon\ area} = \frac{3\pi R^2}{3/2a^2\sqrt{3}}$$

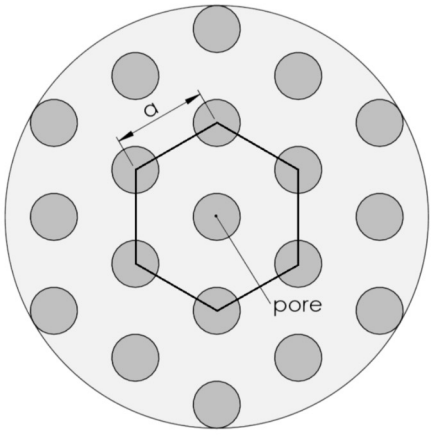

$$\rho = \frac{pore\ area}{square\ area} = \frac{\pi R^2}{a^2}$$

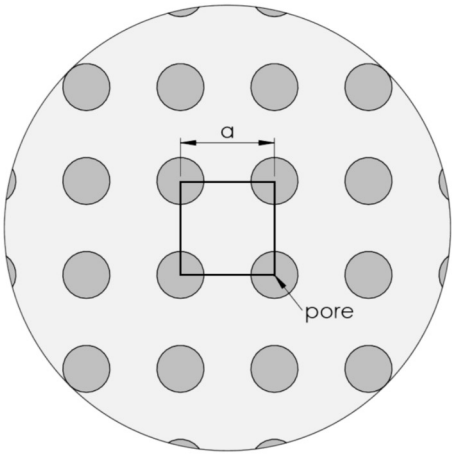

FIG. 1. Schematics of square and hexagonal micropore arrays and formulas to calculate their porosity, where *R* is the radius of a micropore.

ensures the most accurate measurement of the flatness on our system, limited only by the resolution of the Dino microscope (5% margin of error under 200× magnification).

The pulse duration and laser power were measured using an APE PulseCheck autocorrelator and a Coherent LM-3 power meter, respectively. For sample characterization, a Veeco™ NT3300 white light interferometer was used for surface roughness measurements. The hole radius and hole to hole distance was measured with an Olympus BX51™ optical microscope with a JENOPTIC™ ProgResC10 + CCD camera. For postdrilling cleaning, mechanical polishing with an ATM Saphir™ 550 was used. Polishing was

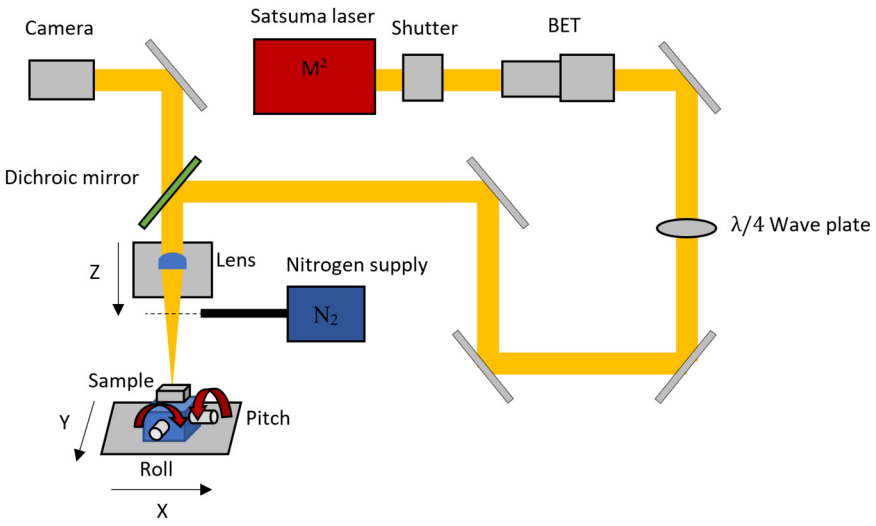

FIG. 2. Schematic of the experimental setup showing the Satsuma ultrafast laser, mechanical shutter, beam expander telescope (BET), λ/4 wave plate, dichroic mirror for inline beam monitoring, camera, focusing lens, pitch and roll stage, XYZ axis motion stage, nitrogen supply, and the sample.

performed on chemcloth with colloidal silica 0.04 μm solution to remove the surface drilling debris. Finally, ultrasonic cleaning in acetone for 15 min was used to remove the drilling debris residing inside the holes and the colloidal silica polishing paste.

After cleaning, the samples were shipped from the University of Cambridge to AFRL/RXAP. Previous measurements of SEY at AFRL/RXAP on 304SS microporous samples showed inconsistencies. However, coating them with an inert thin film material, such as gold, allowed for more consistent and more reliable SEY measurements. This may be due to the postlaser drilling polishing process erratically embedding particles in the surface, and the application of a thin film effectively masks this phenomenon. Thus, all 10 samples had a 100 nm gold film sputter deposited on their surfaces immediately after they were wiped clean with acetone and methanol. The sputtering deposition rate was tracked with a quartz crystal monitor to confirm an accurate film thickness. There is a possibility that the deposited gold did not reach the inner surfaces of the pores, as this was not checked. After the gold deposition was complete, the samples were immediately loaded into vacuum where the SEY measurements were performed.

B. Fabrication results

A total of 10 samples with a micropore array of 4 × 4 mm on a 12 × 12 × 3 mm 304SS with a 100 nm gold film were produced.

TABLE II. Laser drilling parameters for all 10 samples.

Satsuma ultrafast Fiber laser	
Wavelength (nm)	1030
PRF (kHz)	1
Pulse duration (fs)	350
Power (mW)	3.8
Trepanning speed (mm/s)	0.4
Spot size (μm)	4.1
Drilling time p/hole (s)	2

Laser parameters are recorded in Table II. The spot size dictates the in-focus beam parameter used to drill the smallest pores reported in Table I with a pore radius of 8.5 μm. To generate pores of larger radii, the beam was taken out of focus.

The average interferometer roughness measurements of the polished surface area of the samples were found to be Ra ∼ 10.9 nm and Rt ∼ 359 nm prior to gold deposition. The optical microscope images of select samples are available in Fig. 3.

III. EXPERIMENTAL SETUP

The SEY measurements were taken while sustaining a pressure under 10^{-9} Torr. The electron source used is an STAIB Instruments model DESA-150 analyzer with an integrated 0–5 keV electron gun. The vacuum chamber sample holder is rotatable by 360° with a precision of 0.1°, allowing for an oblique angle of incidence primary electron beam measurements. The process for the SEY measurements is shown in a two-step process illustrated in Fig. 4. In step one, the primary electron beam strikes the sample surface and any generated secondary electrons can freely emit from the sample surface. The sample is biased at −20 V to ensure that no tertiary electrons generated from secondary electrons colliding into the vacuum chamber sidewalls absorb into the sample.[15] The sample current is then measured (I_1). In step 2, a +100 V DC bias is applied to the sample. This traps any generated secondary electrons with energies under 100 eV inside the sample. Almost all secondary electrons have energies less than 100 eV; therefore, this is assumed to trap all secondary electrons. The sample current is then measured again (I_2). The SEY (δ) is then calculated with the following formula:

$$\delta = \frac{I_2 - I_1}{I_2}. \quad (1)$$

This process is slightly adjusted from a previous method used to measure SEY from microporous materials,[14] where no bias was applied to the sample in step 1 (now there is a −20 V applied bias).

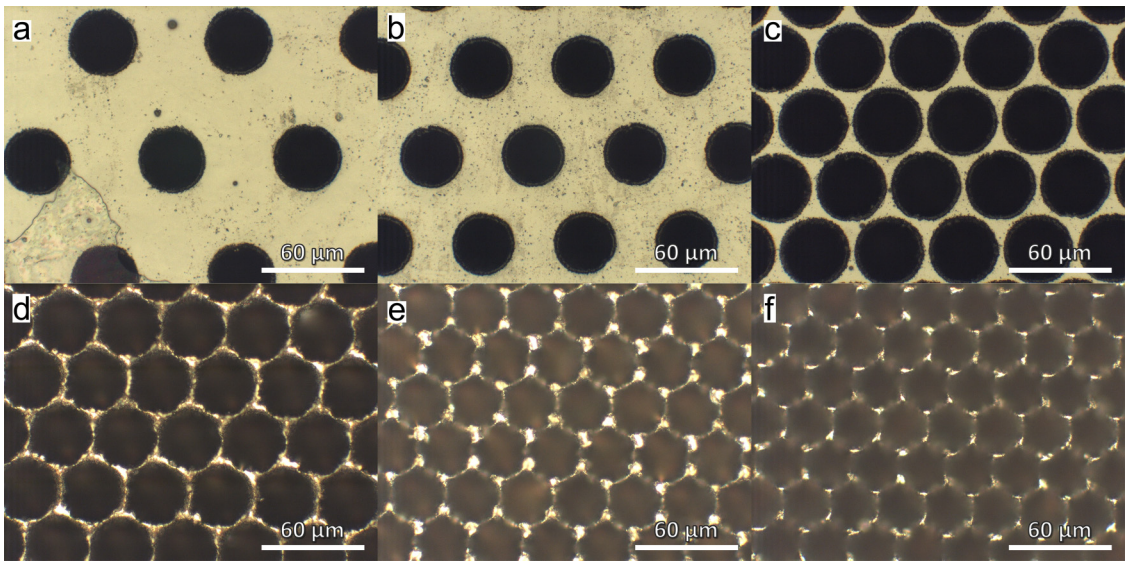

FIG. 3. Optical images of the laser drilled holes in selected 304SS samples prior to 100 nm gold film deposition. Samples 3, 4, 7, 8, 9, and 10 are shown in (a)–(f), respectively.

This inclusion of the negative bias causes a slight systematic increase in the SEY data presented in this work, as the process in step one now rejects more electrons, increasing the current magnitude difference between steps one and two.

To ensure cathode stability, each time immediately before measuring I_1 and I_2, 10 current measurements are taken at 1 s intervals with a constant cathode emission current. If the current drifts more than 10 pA/s (cathode source is emitting ~20 nA current for all measurements), another 10 current measurements are taken, and the current drift is measured again. This process is repeated until the current drift is measured to be below 10 pA/s. This increases the accuracy and consistency of SEY measurements by verifying that there is only negligible current drift between measurements I_1 and I_2.

This SEY measurement process sweeps the energy settings on the electron gun from the lowest to highest energy, while the electron gun is positioned at a constant anode location. At each energy setting, an SEY measurement is taken. This sweep is always repeated twice to isolate any cathode instabilities that persisted long enough to be unobserved in the above cathode stability check. This also ensures that SEY degradation due to continuous electron beam exposure, known as the electron conditioning effect,[16–18] is negligibly affecting the SEY measurements. If the first sweep of measurements varies notably during the subsequent sweep, the data are discarded, and the sweeps are performed again.

Each SEY measurement sweep was averaged across three measurements of arbitrary locations on the anode surface. This is to mitigate the risk of measuring an anomalous location on the anode

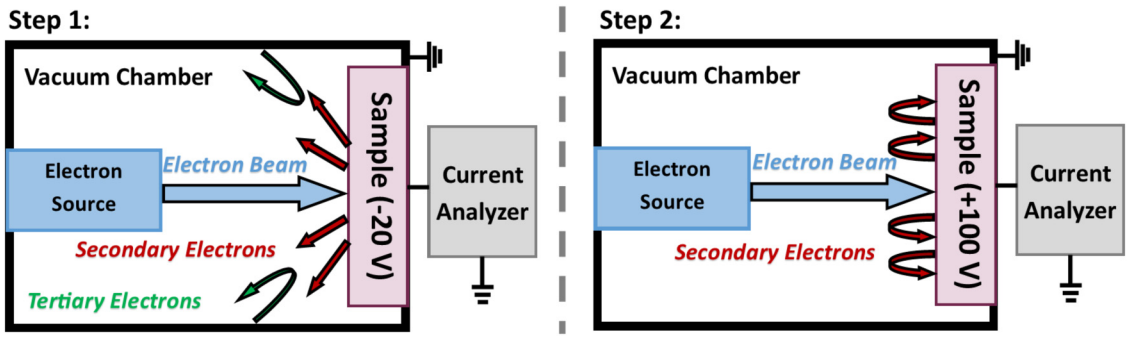

FIG. 4. Diagram of an SEY measurement system.

surface. If at least one measurement sweep differs greatly, then additional measurement sweeps are taken to isolate erroneous data collected from irregular locations on the anode surface.

To ensure that the electron beam diameter is adequately sized to cover a large number of pores, five SEY sweep measurements were taken at five arbitrary locations on the porous region of the lowest porosity sample at a constant electron beam focus setting. The focus was then adjusted, and the above process was repeated until negligible SEY variation was observed across all common energies at all measurement locations. This focus setting was then assumed to generate an adequate beam size for all the micropore SEY measurements reported hereafter.

IV. MODELING AND SIMULATION

A. Empirical SEY model

Our empirical model of SEY for flat surfaces is based on Vaughan's formula[19,20] including additional angle dependent parameters[3] to fit experimental measurements. Unlike the empirical SEY model in Ref. 14, which used two formulas [Eqs. (3a) and (3b) in Ref. 14] to capture the dependence of impact energy of the primary electrons, here we use a single expression, Eq. (2), for all primary impact energies. For an impact of a primary electron upon the surface at an impact angle of θ with respect to the surface normal, the SEY $\delta(\theta)$ of the flat surface is given by the following

TABLE III. Values of fitting coefficients for Eq. (3).

	$w \le 1$	$1 < w \le 3.6$	$w > 3.6$, $\theta < \pi/4$	$w > 3.6$, $\theta \ge \pi/4$
k_{a0}	0.5045	0.3442	0.3505	0.3505
k_{a1}	1	1	1	0.6991
k_{a2}	−0.5772	−0.1376	−2.1390	−1.1600
k_{a3}	1.1180	−1.0200	7.0790	1.1110
k_{a4}	−0.5397	1.6340	−6.8190	0
k_{a5}	−0.0649	−0.7133	0	0
k_{b0}	0.4011	0.3667	0.3642	0.3642
k_{b1}	1	1	1	0.9876
k_{b2}	−0.0394	−0.0415	−1.1400	−0.9825
k_{b3}	0.5863	−0.5305	3.6430	0.7613
k_{b4}	−0.2083	0.5752	−3.5330	0
k_{b5}	−0.1644	−0.1788	0	0

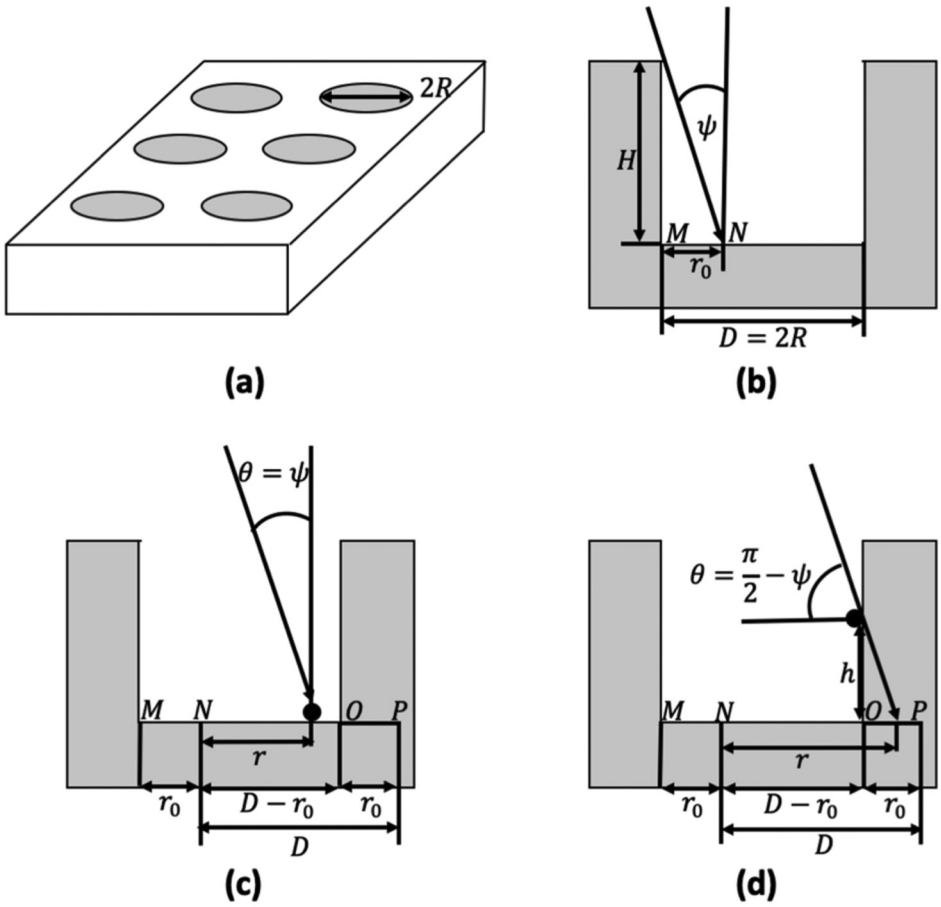

FIG. 5. (a) Schematic of a microporous surface geometry with 3D cylindrical pores. (b) The 2D rectangular well geometry assumed in our MC model. For an incident angle ψ of the primary particles with respect to the normal of the bottom surface, no primary particle can impact on the bottom surface within the length $MN = r_0$. (c) A primary particle impacting the bottom surface at a distance $(r_0 + r)$ from the edge of the well with an impact angle $\theta = \psi$. (d) A primary particle impacting the sidewall at a height h from the bottom surface with an impact angle $\theta = \pi/2 - \psi$.

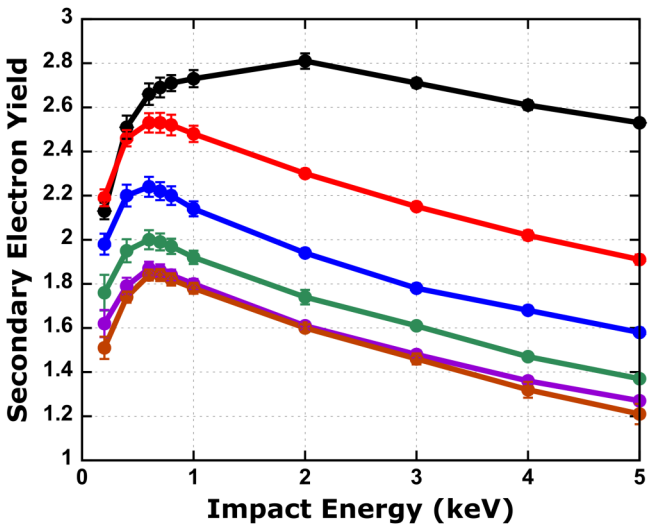

FIG. 6. Measured secondary electron yield as a function of primary electron incidence angle on a nonporous flat gold surface. The curves from bottom to top are represented by 0°, 15°, 30°, 45°, 60°, and 75° incidence angles, respectively.

empirical equation:

$$\frac{\delta(\theta)}{\delta_{max}(\theta)} = w^a e^{1-w^b}. \tag{2}$$

Here, $w = E_i/E_{max}(\theta)$, where E_i is the impact energy of the primary electron. For impacts at an angle θ with respect to the surface normal, where $\theta \in [0, \pi/2]$, the angle-dependent parameters $E_{max}(\theta)$ and $\delta_{max}(\theta)$ are given by

$$E_{max}(\theta) = E_{max0}(1 + k_{sE1}e^{k_{sE2}\theta}), \tag{3a}$$

$$\delta_{max}(\theta) = \delta_{max0}(1 + k_{s\delta1}\theta + k_{s\delta2}\theta^2 + k_{s\delta3}\theta^3 + k_{s\delta4}\theta^4), \tag{3b}$$

where E_{max0} and δ_{max0} are the parameters for normal incidence (i.e., $\theta = 0$) and k_{sE1}, k_{sE2}, $k_{s\delta1}$, $k_{s\delta2}$, $k_{s\delta3}$, and $k_{s\delta4}$ are fitting constants. For the microporous gold surfaces reported in this work, the following empirical values were used for the parameters in Eq. (3): $E_{max0} = 0.6\,\text{kV}$, $\delta_{max0} = 1.84$, $k_{sE1} = 4.129 \times 10^{-6}$, $k_{sE2} = 10.12$, $k_{s\delta1} = -0.035\,66$, $k_{s\delta2} = 0.312$, $k_{s\delta3} = 0.2391$, and $k_{s\delta4} = -0.1694$. The parameters a and b in Eq. (2) are given by

$$a = k_{a0}\,(k_{a1} + k_{a2}\theta + k_{a3}\theta^2 + k_{a4}\theta^3 + k_{a5}\theta^4), \tag{4a}$$

$$b = k_{b0}(k_{b1} + k_{b2}\theta + k_{b3}\theta^2 + k_{b4}\theta^3 + k_{b5}\theta^4). \tag{4b}$$

Here, k_{a0}, k_{a1}, k_{a2}, k_{a3}, k_{a4}, k_{a5}, k_{b0}, k_{b1}, k_{b2}, k_{b3}, k_{b4}, and k_{b5} are fitting coefficients. The values of these fitting coefficients for different values of w and θ are given in Table III.

B. Two-dimensional Monte-Carlo model

After obtaining the empirical SEY model for a flat surface by curve fitting to the experimental measurement as described in Sec. IV A, we employ this SEY model in our MC simulation for the porous surface. In the MC simulation, we model 3D cylindrical pores as 2D rectangular wells in our simulation scheme.[14] We set the height and width of the rectangular well to be H and D, respectively [Fig. 5(b)], where $D = 2R$ corresponds to the diameter of the cylindrical pore [Fig. 5(a)]. We start the simulation by considering $N_0 = 10^4$ particles incident at random locations on the inner surfaces of the rectangular well at an incident angle ψ with respect to the normal of the bottom surface [Fig. 5(b)] with a given impact energy E_i. Each kth particle initially carries $n_{0,k} = 1$ electron.

For a specific incident angle ψ of the primary particles, no primary particle can impact on the bottom surface of the well within the length $MN = r_0$ shown in Fig. 5(b). To determine the random impact location of a primary particle inside the well, we generate a uniform random number r in the range $[0, D]$ which corresponds to the length $NP = D$ in Fig. 5(c). If the generated random number $r < (D - r_0)$ [Fig. 5(c)], then the particle is incident on the bottom surface of the well with an impact angle $\theta = \psi$ at a distance $(r_0 + r)$ from the edge of the well, M. If $r > (D - r_0)$ [Fig. 5(d)], then the particle is incident on the sidewall of the well at a height $h = (r - (D - r_0))/\tan\psi$ from the bottom surface with an impact angle $\theta = \pi/2 - \psi$.

From the empirical model for flat surfaces described above in Eqs. (2)–(4), we calculate the secondary electron yield $\delta_{1,k}$ for each of the primary impacts generating the first generation of secondary particles, each carrying $n_{1,k} = n_{0,k}\delta_{1,k}$ electrons.[14] The emission energy E_0 and emission angle ϕ of the secondary particles are assigned according to the following distributions:[4–6]

$$f(E_0) = \frac{E_0}{E_{0m}^2} e^{-\frac{E_0}{E_{0m}}}, \tag{5}$$

$$g(\phi) = \frac{1}{2}\sin\phi, \tag{6}$$

where $E_{0m} = 0.02E_{max0}$ is the peak of the distribution of emission energies with the expectation value of $E_0 = 2E_{0m}$.

The simulation proceeds by tracking the next generation of secondary particles generated inside the well following the algorithm described in Ref. 14. When all the particles either escape the well or are absorbed by the inner surfaces, the simulation is terminated and the total number of escaping electrons N_e is recorded. The average effective SEY from the rectangular well is then calculated as $\delta_p = N_e/N_0$. The effective SEY of a porous surface is then obtained as[10,13,14]

$$\delta_{surf} = \delta_p\rho + \delta_f(1 - \rho), \tag{7}$$

where ρ is the porosity of the surface and δ_f is the SEY of the flat surface calculated from Eqs. (2)–(4). The SEY model parameters for the flat region, the bottom surface, and the sidewalls of the wells are assumed to be the same.

V. RESULTS

When a primary electron strikes a surface, there are two main factors that limit SEY. First, the energy of the primary electron governs the quantity of secondary electrons generated near the sample surface, with higher energy primary electrons generating more secondary electrons. Second, the depth the primary electron impinges into the sample dictates how many generated secondary electrons can escape out the sample surface. Though higher energy primary electrons may generate more secondary electrons, they also travel to greater depths into the sample, reducing the rate at which secondary electrons can escape out the surface. This is what creates an SEY peak at around primary electron energies of 0.6–2.0 keV in these samples.

Figure 6 shows the SEY evolution across all primary electron angles of incidence for a flat gold sample containing no pores. As the angle of incidence increases, the SEY increases, as reported previously.[18,21,22] This is due to the penetration depth of the primary electrons being reduced by approximately $D(\psi) = D_{\perp}\cos(\psi)$, where ψ is the incidence angle with respect to the normal of the sample surface, $D(\psi)$ is the electron penetration depth as a function of incidence angle, and $D_{\perp}$ is the electron penetration depth for the case of normal incidence. As ψ increases, the secondary electron escape rate is increased due to a decreased penetration distance $D(\psi)$, resulting in an increase in SEY.

Figures 7 and 8 show a comparison of microporous SEY suppression relative to a flat gold surface as a function of increasing ψ for ARs of greater than 3 and about 1.5, respectively. For a small ψ, SEY suppression is close to ubiquitous across all impact energies, reducing SEY as AR or ρ increases, as reported previously.[14] For a large ψ, SEY suppression is very strong for high energies in the high porosity samples but relatively weak near the SEY peak.

Figure 9 shows the SEY evolution for increasing ψ for a high and low porosity sample. This shows that an SEY peak shifts to higher impact energies at large impact angles for only low porosity samples, where the high porosity samples seem to maintain their SEY peak energy throughout all ψ. For the case of the low porosity

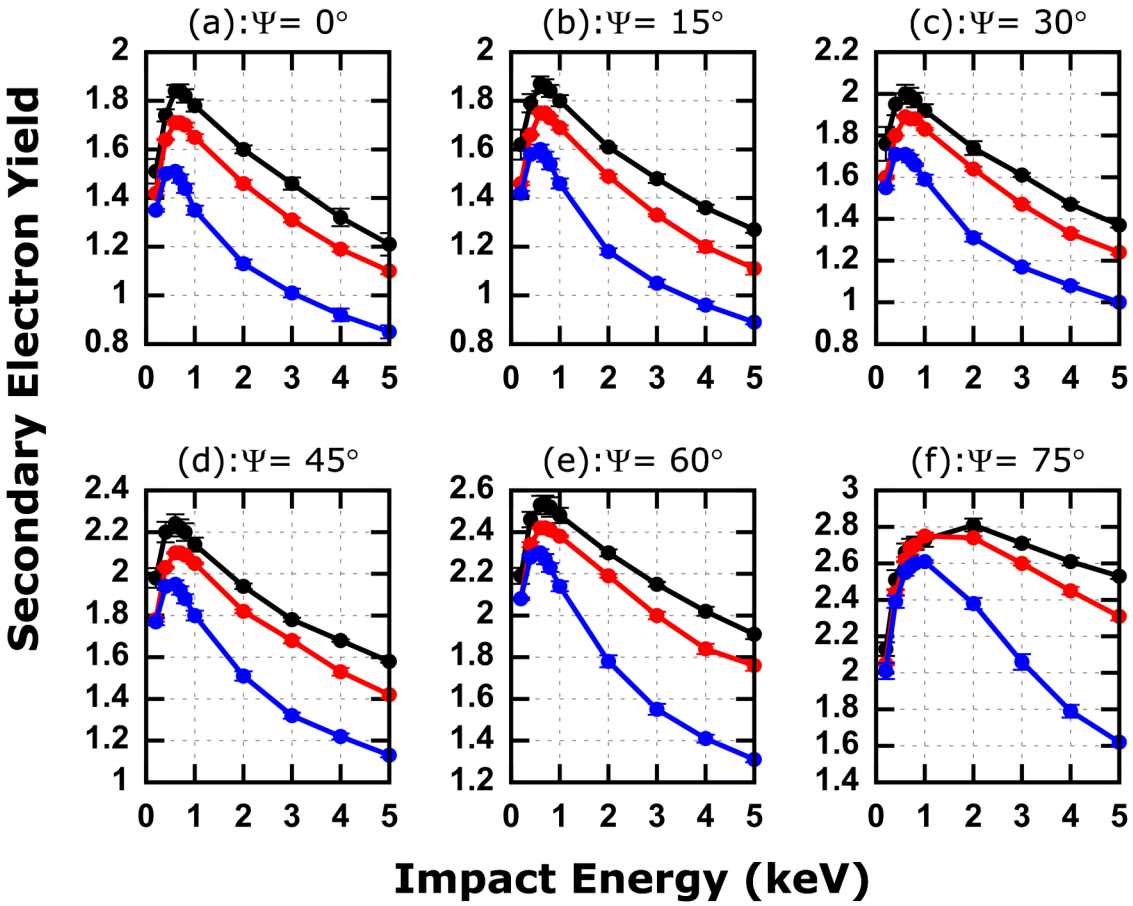

FIG. 7. Measured secondary electron yield as a function of primary electron incidence angle on flat and microporous gold surfaces with ARs > 3 for primary electron incidence angles of (a) $\psi = 0°$, (b) $\psi = 15°$, (c) $\psi = 30°$, (d) $\psi = 45°$, (e) $\psi = 60°$, and (f) $\psi = 75°$. The curves from bottom to top represent sample 6 ($\rho = 0.50$), sample 1 ($\rho = 0.14$), and a flat surface, respectively.

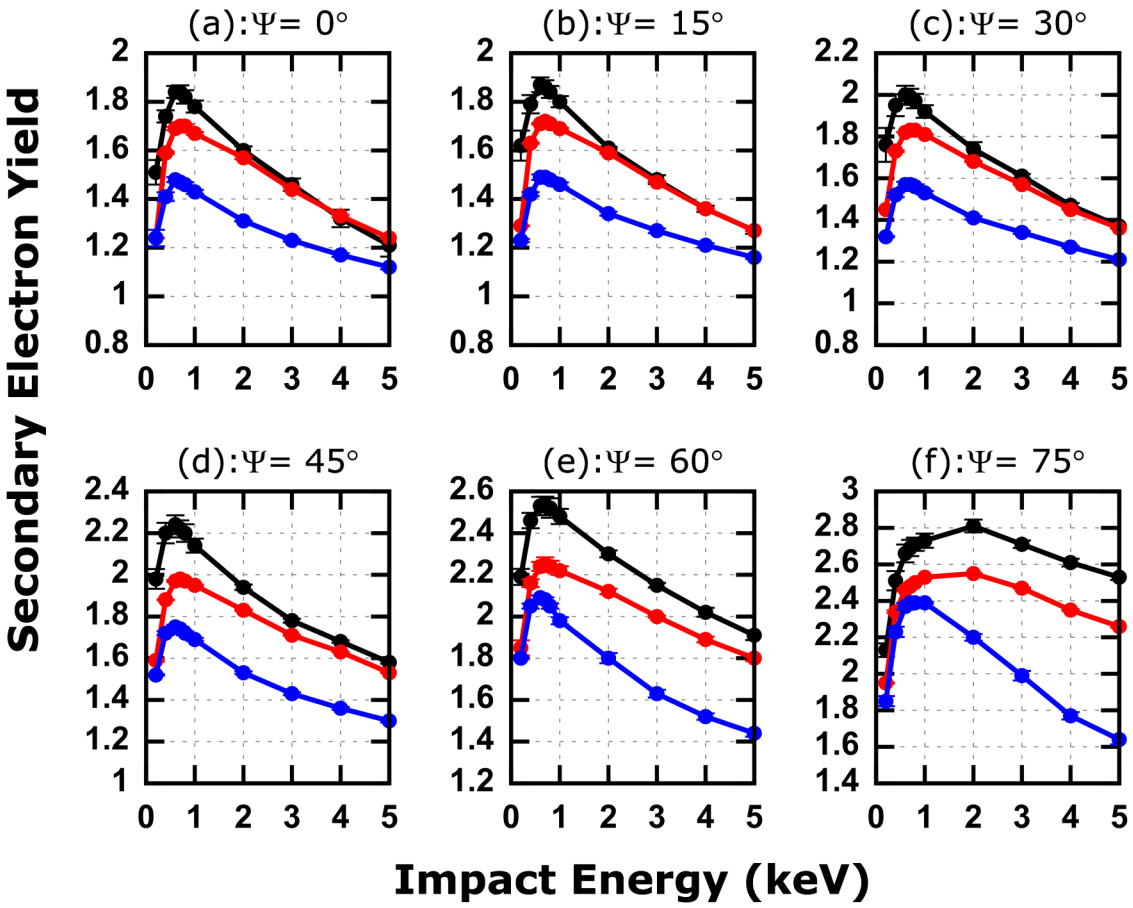

FIG. 8. Measured secondary electron yield as a function of primary electron incidence angle on flat and microporous gold surfaces with ARs of about 1.5 for primary electron incidence angles of (a) $\psi = 0°$, (b) $\psi = 15°$, (c) $\psi = 30°$, (d) $\psi = 45°$, (e) $\psi = 60°$, and (f) $\psi = 75°$. The curves from bottom to top represent sample 7 ($\rho = 0.80$), sample 3 ($\rho = 0.21$), and a flat surface, respectively.

sample, an arbitrary incident electron is likely to strike a nonporous region of the sample. Here, the peak shift phenomenon occurs due to the incident electron penetration depth reduction with increasing incidence angle. Higher energy incident electrons now have greater secondary electron escape rates with their larger secondary electron generation rate. This allows the SEY magnitude at these higher energy locations to supersede the normal incidence SEY maximum, resulting in an SEY peak shift to higher energies. For the case of the high porosity sample, an arbitrary incident electron is now more likely to strike a pore. As incident angle increases, these pores have an increasing probability that an incident electron will strike the pore sidewall, rather than the pore bottom. The angle the electron collides with the pore sidewall is offset by $\theta = 90° - \psi$, as shown in Fig. 5(d). This effect changes the incident electron penetration depth in the pore sidewall to about $D(\psi) = D_{\perp}\sin(\psi)$, negating the SEY peak shift seen in the low porosity samples.

Another interesting feature of Fig. 9 is the dramatic peak SEY increase seen in the high porosity sample as ψ increases from 0° to 75°. This effect seems to only exist near the peak SEY energy. The percent increase in the SEY maximum from $\psi = 0°$ to $\psi = 75°$ is 50% for sample 3 (low porosity, $\rho = 0.21$) and 92% for sample 9 (high porosity, $\rho = 1.0$). This trend can be seen across all the micropore samples, where higher porosities tend to exhibit a sharper peak SEY increase at a large ψ. This is due to the initial impact location of the primary electrons being restricted to shallower pore sidewall depths as ψ increases. Assuming that a primary electron enters the pores directly at the pore center, at $\psi = 75°$, the electron can only traverse a depth of about 13% of the pore diameter before impacting the pore sidewall. This shallow secondary electron generation point results in a substantially reduced SEY suppression when compared to electrons striking the pore bottoms at $\psi = 0°$. This creates a larger disparity in the high porosity SEY peak as ψ increases than seen in low porosity samples, where the dominant secondary generation locations occur outside of the pores. This effect becomes less pronounced as the incident electron impact energies increase away from the SEY peak, as the secondary

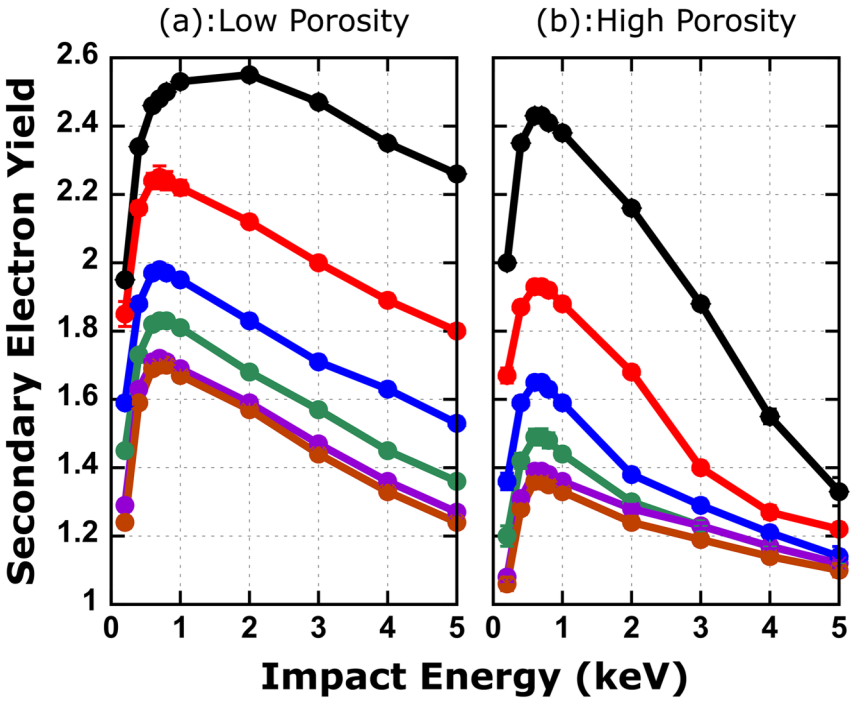

FIG. 9. Measured secondary electron yield as a function of primary electron incidence angle on microporous surfaces. (a) and (b) show sample 3 (low porosity, $\rho = 0.21$) and sample 9 (high porosity, $\rho = 1.0$), respectively. The curves from bottom to top are represented by 0°, 15°, 30°, 45°, 60°, and 75° incidence angles, respectively.

electron escape rate is low for high energy primary electrons impacting the pore sidewall with a large ψ.

Figure 9 shows a monotonic increase in SEY as a function of incidence angle, regardless of porosity. This contradicts a theory by Ye *et al.* stating that there is no monotonic relationship between SEY and incidence angle inside a pore.[11] Though these experimental results do not isolate SEY from an individual pore, the very high porosity samples should effectively represent this, albeit with a

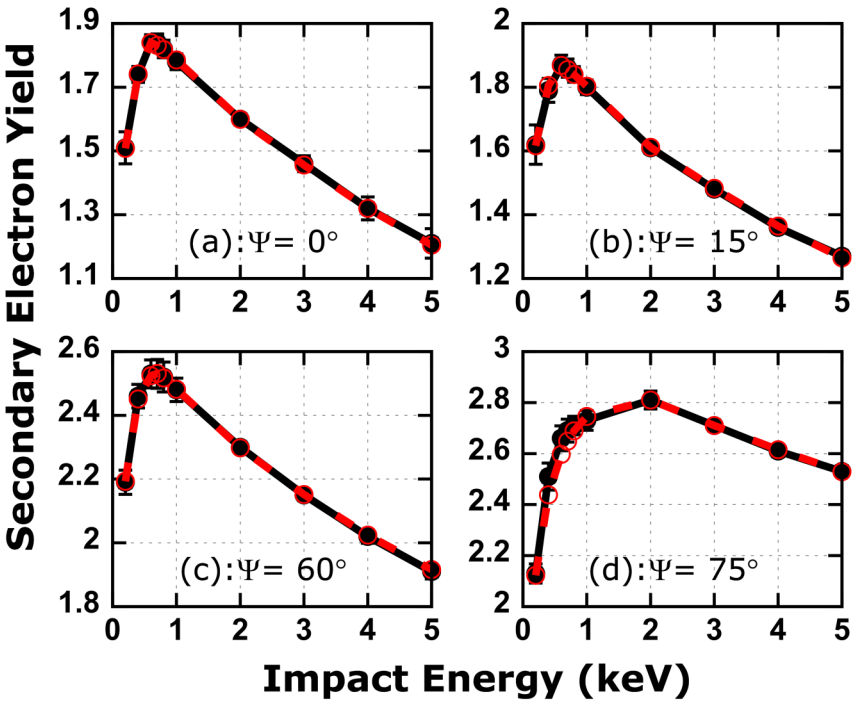

FIG. 10. Measured secondary electron yield compared to the empirical model described in Sec. IV A of a flat (nonporous) gold surface for primary electron incidence angles of (a) $\psi = 0°$, (b) $\psi = 15°$, (c) $\psi = 60°$ and (d) $\psi = 75°$. The measured results and empirical fits are represented by solid black lines and dashed red lines, respectively.

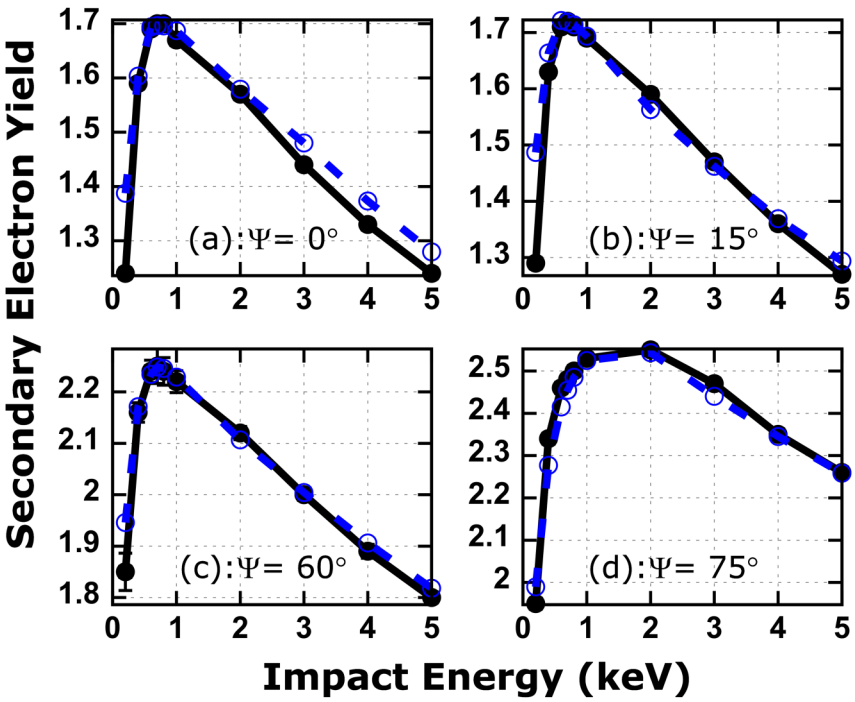

FIG. 11. Measured secondary electron yield compared to the MC model described in Sec. IV B of sample 3 (low porosity $\rho = 0.21$) for primary electron incidence angles of (a) $\psi = 0°$, (b) $\psi = 15°$, (c) $\psi = 60°$, and (d) $\psi = 75°$. The measured and simulation results are represented by solid black lines and dashed blue lines, respectively.

small margin of error due to pore overlap and/or small regions of flat surface between the pores. We speculate that the disagreement with the theoretical results of Ye *et al.* can be attributed to consideration of backscattered electrons. The experiments and simulations conducted in this work neglect backscattered electrons, as their high energies allow them to escape the sample during both steps 1 and 2 of the measurement process, as illustrated in Fig. 4, resulting in a measurement of SEY from only true secondary electrons. The

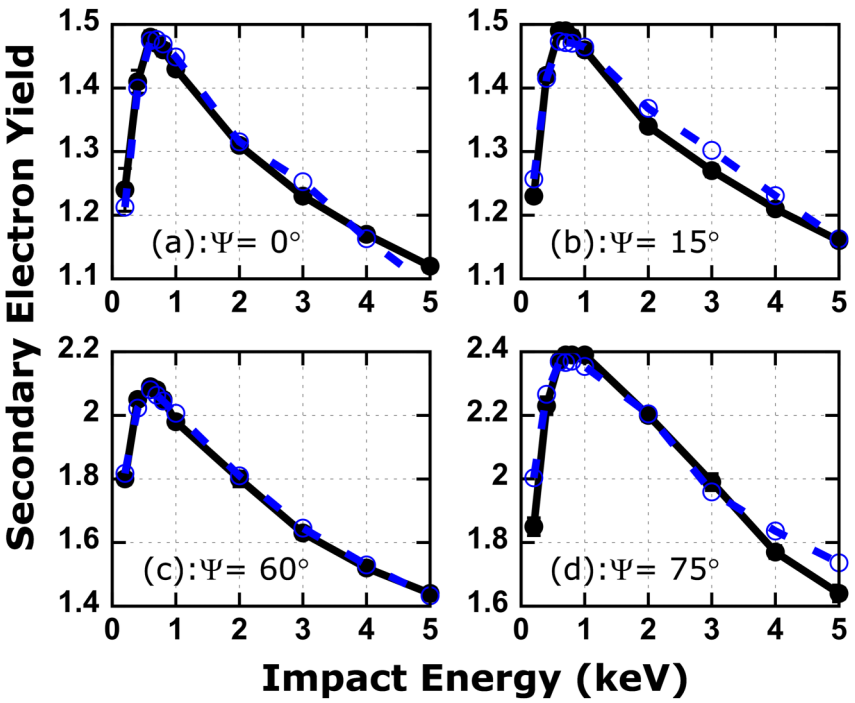

FIG. 12. Measured secondary electron yield compared to the MC model described in Sec. IV B of sample 7 (high porosity, $\rho = 0.79$) for primary electron incidence angles of (a) $\psi = 0°$, (b) $\psi = 15°$, (c) $\psi = 60°$, and (d) $\psi = 75°$. The measured and simulation results are represented by solid black lines and dashed blue lines, respectively.

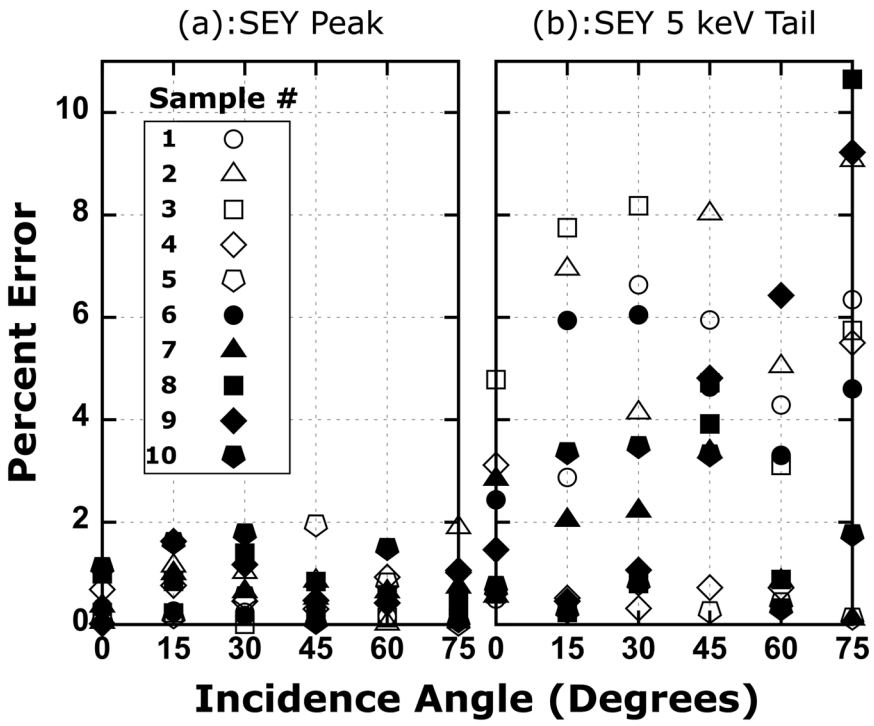

FIG. 13. MC simulation performance at the SEY peak and 5 keV SEY tail for each sample.

simulations from Ye *et al.* consider SEY to be the sum of true secondary electrons and backscattered electrons and considers elastically and inelastically backscattered electron events. At the normal incidence, backscattered electrons will easily escape a pore,[10] while the true secondaries will very effectively be inhibited. The nature of backscattered electron escape patterns could explain the disagreement of the monotonic relation between SEY and incidence angle. Additional experiments considering backscattered electron measurements are needed for further validation.

Figure 10 compares the empirical model from Sec. IV A to the measured results of a flat (nonporous) gold surface across different ψ's. The empirical model is in excellent agreement with the measured results. Figures 11 and 12 compare SEY data of increasing ψ for the MC simulation results to experimental data for samples 3 and 9, respectively. The simulations are in great agreement with the experiment, especially in the energy regime of the SEY maximum. The low porosity simulation results in Fig. 11 exhibit the expected SEY peak shift trend where the SEY maximum shifts to higher energies for a large ψ. The high porosity simulation in Fig. 12 does not exhibit this strong peak shift trend, as expected, and sharply decreases the SEY for energies above the SEY maximum for large ψ.

Figure 13 shows the MC simulation performance at the SEY peak and 5 keV SEY tails for all samples. The performance at the SEY peak is excellent across all samples, retaining all percent errors below 2%. However, the max error threshold rises to ~11% at the 5 keV SEY tail. Deviations of the MC simulations from the measured results are due to the following simulation limitations: (1) not considering effects of energy loss during multigenerations of secondary electron emission, (2) assuming a 2D micropore model, (3) the geometry of the micropores in the experimental samples is not ideally cylindrical, but with a tapered bottom, (4) the SEY in the model is assumed to be the same for the bottom surface and the sidewalls, and (5) the model does not account for pore overlap. Specific reasons for the deviation in different energy regimes can be confirmed with a detailed investigation employing a more complete 3D cylindrical model using tools such as MC or computer simulation technology in the future.

VI. CONCLUSION

In this work, it is shown that deep microporous gold surfaces can be used to suppress SEY for both normal and oblique primary electron incidence angles. Under normal primary electron incidence impacts, the microporous surfaces lead to a reduction of SEY across all impact energies ubiquitously, with a sharper SEY reduction as either the porosity or pore aspect ratio were increased. At sharp oblique angles, the high porosity microporous surfaces were shown to dramatically suppress SEY at high energies above the SEY maximum. However, these high porosity surfaces saw the smallest SEY reduction near the SEY peak. At the normal incidence, the highest porosity sample (sample 10 with $\rho = 1.1$, AR = 1.9) showed the largest peak SEY suppression with a 31% SEY peak reduction relative to the one found for a flat gold surface. At a 75° angle of incidence, sample 7 ($\rho = 0.79$, AR = 1.5) showed the largest peak SEY suppression with a 15% SEY peak reduction compared to the one found for a flat sample. Finally, at a high impact energy of 5 keV and at a 75° angle of incidence, sample 8 ($\rho = 1.0$, AR = 1.7)

showed a dramatic 50% SEY reduction compared to that of a flat gold surface.

A proposed empirical model in this work showed an excellent fit to measured SEY data for different primary electron angles of incidence on a flat gold surface. This model is an improved fit from an earlier proposed empirical model.[14] A 2D MC model for normal incidence primary electron collisions on a microporous surface[14] was improved in this work to include oblique primary electron angles of incidence. The MC model shows excellent agreement with the measured SEY data.

Future research could include developing a 3D MC model with secondary electron energies dependent on the incident electron impact energies. Additional pore shapes and patterns could be investigated, as well as applying these micropore models to more simply fabricated structures with similar morphologies, such as carbon nanotube forests.[23–25] Effects of random surface roughness on SEY could also be studied.[26] Additionally, this research could be implemented into a particle accelerator and HPVE systems to reduce unwanted secondary effects, such as the multipactor effect, in devices for high powered radio frequencies or microwave generation. However, the microporous patterning could potentially reduce surface conductivity in HPVE devices operating at around 100 MHz and higher.

ACKNOWLEDGMENTS

The work was supported by the Air Force Office of Scientific Research (USAFOSR) under Award Nos. FA9550-18-1-0061 and FA9550-18-1-0062. A. Iqbal gratefully acknowledges support from an MIPSE Graduate Fellowship. J. Ludwick received funding from the State of Ohio through the Dayton Area Graduate Studies Institute (DAGSI) program, under Contract No. FA8650-12-2-7248 (R22021, Topic No. RX15-10).

REFERENCES

[1]M. Furman and M. Pivi, Phys. Rev. ST Accel. Beams **5**, 124404 (2002).
[2]N. Balcon, D. Payan, M. Belhaj, T. Tondu, and V. Inguimbert, IEEE Trans. Plasma Sci. **40**, 282 (2012).
[3]J. R. M. Vaughan, IEEE Trans. Electron Devices **35**, 1172 (1988).
[4]R. A. Kishek and Y. Y. Lau, Phys. Rev. Lett. **80**, 4 (1998).
[5]P. Zhang, Y. Y. Lau, M. Franzi, and R. M. Gilgenbach, Phys. Plasmas **18**, 053508 (2011).
[6]A. Iqbal, J. Verboncoeur, and P. Zhang, Phys. Plasmas **25**, 043501 (2018).
[7]A. Iqbal, J. Verboncoeur, and P. Zhang, Phys. Plasmas **26**, 024503 (2019).
[8]D. C. Joy, Scanning **17**, 270 (2006).
[9]M. Pivi, F. K. King, R. E. Kirby, T. O. Raubenheimer, G. Stupakov, and F. Le Pimpec, J. Appl. Phys. **104**, 104904 (2008).
[10]M. Ye, Y. N. He, S. G. Hu, R. Wang, T. C. Hu, J. Yang, and W. Z. Cui, J. Appl. Phys. **113**, 104905 (2013).
[11]M. Ye, Y. N. He, S. G. Hu, J. Yang, R. Wang, T. C. Hu, W. B. Peng, and W. Z. Cui, J. Appl. Phys. **114**, 104905 (2013).
[12]M. Ye, D. Wang, and Y. He, J. Appl. Phys. **121**, 124901 (2017).
[13]J. M. Sattler, R. A. Coutu, R. Lake, T. Laurvick, T. Back, and S. Fairchild, J. Appl. Phys. **122**, 055304 (2017).
[14]A. Iqbal, J. Ludwick, S. Fairchild, M. Cahay, D. Gortat, M. Sparkes, W. O'Neill, T. C. Back, and P. Zhang, J. Vac. Sci. Technol, B **38**, 013801 (2020).
[15]R. E. Kirby and S. Linear, SLAC-PUB-10541, see http://inspirehep.net/record/654496/ (2004).
[16]R. Cimino, M. Commisso, D. R. Grosso, T. Demma, V. Baglin, R. Flammini, and R. Larciprete, Phys. Rev. Lett. **109**, 064801 (2012).
[17]B. Henrist, N. Hilleret, C. Scheuerlein, M. Taborelli, and G. Vorlaufer, "The variation of the secondary electron yield and of the desorption yield of copper under electron bombardment: Origin and impact on the conditioning of the LHC," in 8th European Particle Accelerator Conference (EPAC), Paris, France, 3–7 June 2002, p. 2553.
[18]R. E. Kirby and F. K. King, Nucl. Instrum. Methods A **469**, 1 (2001).
[19]J. R. M. Vaughan, IEEE Trans. Electron Devices **36**, 1963 (1989).
[20]J. R. M. Vaughan, IEEE Trans. Electron Devices **40**, 830 (1993).
[21]N. Bundaleski, M. Belhaj, T. Gineste, and O. M. N. D. Teodoro, in *2013 IEEE 14th International Vacuum Electronics Conference IVEC*, Paris, France, 21–23 May 2013 (IEEE, Paris, France, 2013), pp. 1–2.
[22]A. Shih and C. Hor, IEEE Trans. Electron Devices **40**, 824 (1993).
[23]Md. K. Alam, P. Yaghoobi, and A. Nojeh, Scanning **31**, 221 (2009).
[24]M. K. Alam, P. Yaghoobi, and A. Nojeh, J. Vac. Sci. Technol. B **28**, C6J13 (2010).
[25]B. Wood, J. Lee, G. Wilson, T.-C. Shen, and J. R. Dennison, IEEE Trans. Plasma Sci. **47**, 3801 (2019).
[26]C. Watts, M. Gilmore, and E. Schamiloglu, IEEE Trans. Plasma Sci. **39**, 836 (2011).